

Data Space Inversion for Efficient Predictions and Uncertainty Quantification for Geothermal Models

Alex de Beer¹, Andrew Power¹, Daniel Wong¹, Ken Dekkers¹,
Michael Gravatt¹, John P. O’Sullivan¹, Michael J. O’Sullivan¹,
Oliver J. Maclaren¹, and Ruanui Nicholson¹

¹Department of Engineering Science and Biomedical Engineering, University of Auckland, Auckland 1010,
New Zealand

Key Points:

- We review data space inversion (DSI), an efficient method for making model predictions with quantified uncertainty, in a geothermal context
- We provide a thorough evaluation of the DSI framework using two model problems arising in geothermal reservoir engineering
- Our results show that DSI can produce accurate predictions at a significantly lower computational cost than other conventional methods

arXiv:2407.15401v1 [stat.AP] 22 Jul 2024

Abstract

The ability to make accurate predictions with quantified uncertainty provides a crucial foundation for the successful management of a geothermal reservoir. Conventional approaches for making predictions using geothermal reservoir models involve estimating unknown model parameters using field data, then propagating the uncertainty in these estimates through to the predictive quantities of interest. However, the unknown parameters are not always of direct interest; instead, the predictions are of primary importance. Data space inversion (DSI) is an alternative methodology that allows for the efficient estimation of predictive quantities of interest, with quantified uncertainty, that avoids the need to estimate model parameters entirely. In this paper, we evaluate the applicability of DSI to geothermal reservoir modelling. We first review the processes of model calibration, prediction and uncertainty quantification from a Bayesian perspective, and introduce data space inversion as a simple, efficient technique for approximating the posterior predictive distribution. We then apply the DSI framework to two model problems in geothermal reservoir modelling. We evaluate the accuracy and efficiency of DSI relative to other common methods for uncertainty quantification, study how the number of reservoir model simulations affects the resulting approximation to the posterior predictive distribution, and demonstrate how the framework can be enhanced through the use of suitable reparametrisations. Our results support the idea that data space inversion is a simple, robust and efficient technique for making predictions with quantified uncertainty using geothermal reservoir models, providing a useful alternative to more conventional approaches.

1 Introduction

Computational models are widely used in geothermal reservoir engineering to facilitate effective decision making (O’Sullivan & O’Sullivan, 2016). One of the key features of these models is the ability to make predictions with quantified uncertainty. Computing accurate predictions and uncertainty estimates generally requires calibration of the model; that is, the estimation of model parameters, such as the subsurface permeability structure and the strength and location of the deep mass upflows at the base of the system, using observations such as downhole temperature and pressure measurements. In many situations, the parameters themselves are not of direct interest; instead, the predictions are of primary importance. However, the calibration process is typically the most computationally demanding step in the process of making predictions.

Here we discuss the application of the data space inversion (DSI) methodology (Sun & Durlofsky, 2017; Sun et al., 2017) for making predictions as well as providing associated estimates of uncertainty. The DSI framework provides several computational advantages, the most significant being the ability to effectively circumvent the calibration process; rather, it simply estimates the values of predictive quantities of interest conditioned on measured data. This idea is sometimes referred to as *direct forecasting*. Furthermore, the DSI approach does not require access to model derivatives (in fact, the method can be applied to non-differentiable models) while much of the required computation can be carried out in parallel. The DSI approach has been used successfully in a variety of applications, including subsurface hydrology (Delottier et al., 2023; Jiang et al., 2020; Jiang & Durlofsky, 2021; Wu et al., 2021) and petroleum engineering (Lima et al., 2020; Liu et al., 2021). The application of the framework to geothermal reservoir modelling, however, is largely unexplored and potentially more challenging as the governing equations are generally highly nonlinear in the geothermal context, with simulation non-convergence being a common issue (see, e.g., Croucher et al. (2020); O’Sullivan et al. (2013)).

We note that the idea of direct forecasting is not exclusive to DSI; in particular, the Bayesian evidential learning (BEL) framework (Scheidt et al., 2018) also involves direct forecasting. Like DSI, the BEL framework has been applied in a variety of subsur-

face modelling applications (Hermans et al., 2018; Michel et al., 2020; Pradhan & Mukerji, 2020); most notably, Athens and Caers (2019) demonstrate the application of BEL to predict the temperature in a geothermal target area of a synthetic model based on Dixie Valley, Nevada. We note, however, that only single-phase, natural state simulations are considered in this study; by contrast, we apply the DSI framework to a two-phase problem, and consider both natural state and production history simulations.

In this paper, we build on our previous work (Power et al., 2022) to investigate the applicability of the DSI methodology to geothermal reservoir modelling. We consider two synthetic model problems (outlined in Section 3); one based on a simplified two-dimensional reservoir and one based on a large-scale, transient three-dimensional reservoir. Through these model problems, we provide a numerical comparison between the DSI framework and other methods for uncertainty quantification in subsurface modelling, investigate how the number of reservoir model simulations affects the resulting approximation to the posterior predictive distribution, and illustrate the value of applying suitable transformations to the observations or predictive quantities of interest prior to the use of the DSI framework.

Before introducing the DSI framework, we briefly recall the key concepts and steps involved in a typical (Bayesian) statistical approach to geothermal model calibration and prediction, and the associated uncertainty quantification.

2 Methodology

We first introduce some important notation used throughout the remainder of this paper. We reserve bold lowercase letters for vectors (i.e., $\mathbf{v} \in \mathbb{R}^n$) and bold uppercase letters for matrices (i.e., $\mathbf{A} \in \mathbb{R}^{n \times m}$). For a symmetric positive definite matrix $\mathbf{G} \in \mathbb{R}^{n \times n}$ and vector $\mathbf{v} \in \mathbb{R}^n$, we let $\|\mathbf{v}\|_{\mathbf{G}}$ denote the weighted Euclidean norm; i.e., $\|\mathbf{v}\|_{\mathbf{G}} := \sqrt{\mathbf{v}^\top \mathbf{G} \mathbf{v}}$. Finally, we denote by $\mathcal{N}(\mathbf{v}_0, \mathbf{G})$ the Gaussian (normal) distribution with mean \mathbf{v}_0 and (proper) covariance matrix $\mathbf{G} \in \mathbb{R}^{n \times n}$.

We now provide a brief review of the standard approach to quantifying uncertainty in geothermal model predictions, as well as the DSI methodology. Uncertainty quantification (UQ) for geothermal reservoir models typically uses a Bayesian framework (Kaipio & Somersalo, 2006; Tarantola, 2005) as it naturally allows for incorporation and quantification of various sources and types of uncertainty. The typical procedure is as follows:

1. Calibrate (i.e., estimate) the model parameters using data.
2. Approximately (i.e., linearly) quantify the posterior uncertainty in the parameters.
3. Propagate the posterior parameter uncertainty to the predictive quantities of interest.

We now provide a detailed outline of each of these steps.

2.1 Calibration

Calibration of geothermal reservoir models is typically based on assuming (or at least approximating) the parameters and data are linked by a setup of the form

$$\mathbf{d}^{\text{obs}} = \mathbf{f}(\mathbf{k}) + \mathbf{e}, \quad (1)$$

where $\mathbf{d}^{\text{obs}} \in \mathbb{R}^d$ denotes the data, $\mathbf{k} \in \mathbb{R}^n$ denotes the unknown parameters, $\mathbf{f} : \mathbb{R}^n \rightarrow \mathbb{R}^d$ represents the forward model (sometimes referred to as the *parameter-to-observable* mapping; see Section 3.1 for details), and $\mathbf{e} \in \mathbb{R}^d$ denotes measurement error (as well as possible model error).

As pointed out previously, UQ for geothermal models is typically considered using the Bayesian framework. Within this framework, the calibration problem is recast as a problem of statistical inference, where the goal is to estimate the (parameter) posterior distribution $\pi(\mathbf{k}|\mathbf{d})$; that is, the conditional distribution of the parameters given the measured data. The posterior distribution can be expressed using Bayes' theorem,

$$\pi(\mathbf{k}|\mathbf{d}) = \frac{\pi(\mathbf{d}^{\text{obs}}|\mathbf{k})\pi(\mathbf{k})}{\pi(\mathbf{d}^{\text{obs}})} \propto \pi(\mathbf{d}^{\text{obs}}|\mathbf{k})\pi(\mathbf{k}).$$

Assuming the errors, \mathbf{e} , are independent of the parameters, \mathbf{k} , it is well known (see, e.g., Calvetti and Somersalo (2007); Kaipio and Somersalo (2006)), that the likelihood inherits the distribution of the noise; that is, $\pi(\mathbf{d}^{\text{obs}}|\mathbf{k}) = \pi_e(\mathbf{d}^{\text{obs}} - \mathbf{f}(\mathbf{k}))$. The resulting posterior distribution is given by

$$\pi(\mathbf{k}|\mathbf{d}^{\text{obs}}) \propto \pi(\mathbf{d}^{\text{obs}}|\mathbf{k})\pi(\mathbf{k}) = \pi_e(\mathbf{d}^{\text{obs}} - \mathbf{f}(\mathbf{k}))\pi(\mathbf{k}).$$

The prior density $\pi(\mathbf{k})$ describes our beliefs about the parameters before (i.e., prior to) considering the data, while the likelihood $\pi_e(\mathbf{d}^{\text{obs}} - \mathbf{f}(\mathbf{k}))$ encodes the likelihood of the data given the parameter.

Assuming *a priori*, as is standard, the parameters and errors are normally distributed—that is, $\mathbf{k} \sim \mathcal{N}(\mathbf{k}_0, \mathbf{\Gamma}_k)$ and $\mathbf{e} \sim \mathcal{N}(\mathbf{0}, \mathbf{\Gamma}_e)$ —the posterior can be written as (Calvetti & Somersalo, 2007; Kaipio & Somersalo, 2006)

$$\pi(\mathbf{k}|\mathbf{d}^{\text{obs}}) \propto \exp \left\{ -\frac{1}{2} \left(\left\| \mathbf{d}^{\text{obs}} - \mathbf{f}(\mathbf{k}) \right\|_{\mathbf{\Gamma}_e^{-1}}^2 + \left\| \mathbf{k} - \mathbf{k}_0 \right\|_{\mathbf{\Gamma}_k^{-1}}^2 \right) \right\}. \quad (2)$$

Computing a full characterisation of the posterior generally requires the use of sampling-based approaches such as Markov chain Monte Carlo (MCMC) (Cui et al., 2011, 2019; Maclaren et al., 2020; Scott et al., 2022). However, for most geothermal models these methods are computationally infeasible. As a computationally cheaper alternative, it is common to compute the *maximum a posteriori* (MAP) estimate, \mathbf{k}_{MAP} ; that is, the point in parameter space which maximises the posterior density. The MAP estimate is defined as

$$\mathbf{k}_{\text{MAP}} := \arg \min_{\mathbf{k} \in \mathbb{R}^n} \left\{ \frac{1}{2} \left\| \mathbf{d}^{\text{obs}} - \mathbf{f}(\mathbf{k}) \right\|_{\mathbf{\Gamma}_e^{-1}}^2 + \frac{1}{2} \left\| \mathbf{k} - \mathbf{k}_0 \right\|_{\mathbf{\Gamma}_k^{-1}}^2 \right\}. \quad (3)$$

Calibration of a geothermal model within the Bayesian framework is thus synonymous with computing the MAP estimate. Due to the scale and computational complexity of a typical geothermal model, computing the MAP estimate can require a significant amount of time, even when efficient methods such as adjoint-based approaches are used (Bjarkason et al., 2018, 2019; Gonzalez-Gutierrez et al., 2018).

2.2 Approximate Parameter Uncertainty Quantification

After computing the MAP estimate, it is common to quantify the posterior uncertainty approximately using a local Gaussian approximation (Omagbon et al., 2021; Zhang et al., 2014); that is, $\pi(\mathbf{k}|\mathbf{d}^{\text{obs}}) \approx \mathcal{N}(\mathbf{k}_{\text{MAP}}, \mathbf{\Gamma}_{\text{post}})$. A common approximation to the posterior covariance matrix is given by (see, e.g., Omagbon et al. (2021))

$$\mathbf{\Gamma}_{\text{post}} = (\mathbf{F}^\top \mathbf{\Gamma}_e^{-1} \mathbf{F} + \mathbf{\Gamma}_k^{-1})^{-1}, \quad (4)$$

where \mathbf{F} denotes the sensitivity (Jacobian) matrix of the model with respect to the parameters evaluated at the MAP estimate; $F_{ij} = \partial f_i / \partial k_j$, for $i = 1, 2, \dots, d$ and $j = 1, 2, \dots, n$. Samples from the Gaussian approximation to the posterior, $\mathcal{N}(\mathbf{k}_{\text{MAP}}, \mathbf{\Gamma}_{\text{post}})$ can be generated as

$$\mathbf{k}^{\text{samp}} = \mathbf{k}_{\text{MAP}} + \mathbf{L}_{\text{post}} \boldsymbol{\eta}^{\text{samp}}, \quad (5)$$

where $\mathbf{L}_{\text{post}}\mathbf{L}_{\text{post}}^\top = \mathbf{\Gamma}_{\text{post}}$, and $\boldsymbol{\eta}^{\text{samp}}$ is a sample from the n -dimensional standard Gaussian distribution; that is, $\boldsymbol{\eta}^{\text{samp}} \sim \mathcal{N}(\mathbf{0}, \mathbf{I})$.

We note that there exist several additional classes of methods that have been used to approximate the parameter posterior and posterior predictive distributions in geothermal settings. One such method is randomised maximum likelihood (RML; Kitanidis (1995); Oliver et al. (1996)), in which a set of stochastic optimisation problems are solved to obtain samples distributed in regions of high posterior density (see, e.g., Tian et al. (2024); Türeyen et al. (2014); Zhang et al. (2014)). These optimisation problems take the same form as Equation (3), but the data is perturbed using a sample from the distribution of the error and the prior mean is replaced by a sample from the prior. While RML generally produces a more accurate approximation to the posterior than linearisation about the MAP estimate, the computational expense is amplified given that each sample from the (approximate) posterior incurs a similar computational cost to computing the MAP estimate. An alternative class of methods are ensemble methods (Y. Chen & Oliver, 2013; Emerick & Reynolds, 2013; Iglesias et al., 2013), which are based on sampling methods such as RML, but employ an ensemble (sample-based) approximation of any required derivative or covariance information (see, e.g., Békési et al. (2020); Bjarkason et al. (2020)). These are simpler to implement and can be less computationally intensive than methods such as RML; however, the calibration process is still iterative and potentially requires many forward simulations.

2.3 Approximate Predictive Uncertainty Quantification

Carrying out uncertainty quantification for the predictive quantities of interest, denoted here by $\mathbf{p} \in \mathbb{R}^m$, relies on having a *predictive model*, $\mathbf{q} : \mathbb{R}^n \rightarrow \mathbb{R}^m$, relating the parameters to the predictions; that is,

$$\mathbf{p} = \mathbf{q}(\mathbf{k}). \quad (6)$$

We note that in various settings, the forward model $\mathbf{f}(\cdot)$ and predictive model $\mathbf{q}(\cdot)$ may be represented by the same model but evaluated at different locations in space and/or time. In any case, to propagate the uncertainty from the parameters through to the predictions, typically one of two methods is applied (Omagbon et al., 2021):

1. Samples from the (approximate) parameter posterior are generated (see Equation (5)) and are run through \mathbf{q} to give prediction samples, i.e., $\mathbf{q}(\mathbf{k}^{(i)})$ where $\mathbf{k}^{(i)} \sim \mathcal{N}(\mathbf{k}_{\text{MAP}}, \mathbf{\Gamma}_{\text{post}})$.
2. A Gaussian approximation of the posterior predictive distribution is made; that is, $\mathbf{p} \sim \mathcal{N}(\mathbf{p}_0, \mathbf{\Gamma}_{\text{pred}})$, with

$$\mathbf{p}_0 = \mathbf{q}(\mathbf{k}_{\text{MAP}}), \quad \mathbf{\Gamma}_{\text{pred}} = \mathbf{Q}\mathbf{\Gamma}_{\text{post}}\mathbf{Q}^\top, \quad (7)$$

where \mathbf{Q} denotes the sensitivity (Jacobian) matrix of the predictive model with respect to parameters, i.e., $Q_{ij} = \partial q_i / \partial k_j$ for $i = 1, 2, \dots, m$ and $j = 1, 2, \dots, n$, evaluated at the MAP estimate.

The latter approach is often termed *linear(-ised) uncertainty propagation* and may not be suitable in all situations; see Omagbon et al. (2021) for a comparison and more in-depth discussion of these two approaches within the geothermal context. We emphasise that both of the aforementioned approaches only approximate the posterior predictive distribution (with the exception of the case where both the forward and predictive models are linear and the prior and error distributions are both Gaussian).

2.4 Accurate Predictive Uncertainty Quantification

Although infeasible in most geothermal settings, it is theoretically possible to accurately characterise the posterior predictive distribution. Specifically, this involves first

generating samples from the true posterior using (for example) MCMC, then running these samples through the predictive model. In this work, we use this approach to provide a benchmark for the simplified two-dimensional reservoir (see Section 3.2).

2.5 The Data Space Inversion Approach

The main computational bottleneck associated with the standard procedure for uncertainty quantification is computation of the MAP estimate, \mathbf{k}_{MAP} ; this requires the solution of a (typically) high dimensional optimisation problem constrained by the non-linear governing equations. By contrast, the DSI framework essentially (approximately) marginalises over the uncertain parameters \mathbf{k} to focus on the posterior predictive distribution. This is natural when the prediction and associated uncertainties are of primary interest, as is common in geothermal settings, and avoids the need to compute the MAP estimate altogether. The DSI process is now outlined, while pseudocode is provided in Algorithm 1.

Initially a set of samples, $\{\mathbf{k}_i\}_{i=1}^\ell$, from are drawn from the prior and are run through both the forward and predictive models, giving the ensemble of triples: $\{(\mathbf{k}_i, \mathbf{d}_i, \mathbf{p}_i)\}_{i=1}^\ell$, where $\mathbf{d}_i = \mathbf{f}(\mathbf{k}_i)$ and $\mathbf{p}_i = \mathbf{q}(\mathbf{k}_i)$. From this ensemble a sample covariance matrix is computed,

$$\begin{bmatrix} \mathbf{\Gamma}_d & \mathbf{\Gamma}_{dp} \\ \mathbf{\Gamma}_{pd} & \mathbf{\Gamma}_p \end{bmatrix} \approx \frac{1}{\ell-1} \mathbf{C} \mathbf{C}^\top, \quad \mathbf{C} = \begin{bmatrix} \mathbf{d}_1 - \mathbf{d}_0 & \mathbf{d}_2 - \mathbf{d}_0 & \cdots & \mathbf{d}_\ell - \mathbf{d}_0 \\ \mathbf{p}_1 - \mathbf{p}_0 & \mathbf{p}_2 - \mathbf{p}_0 & \cdots & \mathbf{p}_\ell - \mathbf{p}_0 \end{bmatrix}, \quad (8)$$

$$\mathbf{d}_0 \approx \frac{1}{\ell} \sum_{i=1}^\ell \mathbf{d}_i, \quad \mathbf{p}_0 \approx \frac{1}{\ell} \sum_{i=1}^\ell \mathbf{p}_i. \quad (9)$$

The conditional mean and conditional covariance of the predictions conditioned on the measured data can then be computed, respectively, as

$$\mathbf{p}_{0|d^{\text{obs}}} = \mathbf{p}_0 + \mathbf{\Gamma}_{pd} \mathbf{\Gamma}_{d+e}^{-1} (\mathbf{d}^{\text{obs}} - \mathbf{d}_0), \quad \mathbf{\Gamma}_{p|d^{\text{obs}}} = \mathbf{\Gamma}_p - \mathbf{\Gamma}_{pd} \mathbf{\Gamma}_{d+e}^{-1} \mathbf{\Gamma}_{dp}, \quad \mathbf{\Gamma}_{d+e} = \mathbf{\Gamma}_d + \mathbf{\Gamma}_e. \quad (10)$$

Furthermore, samples from the conditional posterior predictive distribution can be computed in a similar manner to the prior samples (see Eq. (5)). Specifically, taking $\boldsymbol{\xi}$ as an m -dimensional standard Gaussian random variable, i.e. $\boldsymbol{\xi} \sim \mathcal{N}(\mathbf{0}, \mathbf{I})$, and computing $\mathbf{L}_{p|d^{\text{obs}}}$ such that $\mathbf{L}_{p|d^{\text{obs}}} \mathbf{L}_{p|d^{\text{obs}}}^\top = \mathbf{\Gamma}_{p|d^{\text{obs}}}$, a sample \mathbf{p}^{samp} can be simulated by computing

$$\mathbf{p}^{\text{samp}} | \mathbf{d}^{\text{obs}} = \mathbf{p}_{0|d^{\text{obs}}} + \mathbf{L}_{p|d^{\text{obs}}} \boldsymbol{\xi}^{\text{samp}}. \quad (11)$$

Remark 1 *In general, the DSI methodology provides only an approximation to the posterior predictive distribution of the quantities of interest (QoIs). However, the accuracy and stability of this approximation is clearly dependent on the number of samples used to estimate the covariance matrix and means in Equations (8) and (9), respectively. It is useful to note that the simulations for each sample can be carried out in parallel and, importantly, that these simulations can be carried out offline; that is, before the collection of any data. Once the covariance matrices have been computed (and stored), conditioning on the data is essentially trivial, requiring only matrix operations (see Equations (10) and (11)).*

2.6 Reparametrisations

The DSI method outlined above can be understood as the construction of a Gaussian surrogate model between the data and predictive quantities of interest (QoIs). In various cases, the assumption (or approximation) of the data or predictive QoIs being Gaussian is unwarranted, and it can be advantageous to reparametrise (i.e., transform)

these quantities, or some subset of them; see, for example, the works of Jiang et al. (2021); Manewell et al. (2024); Sun and Durlofsky (2017); Sun et al. (2017), or the numerical example in Section 3.3.

We end this section by providing the associated pseudocode for implementing the DSI method; this is outlined in Algorithm 1.

Algorithm 1 Data space inversion

Require: $\pi(\mathbf{k})$, Γ_e , $\mathbf{f}(\cdot)$, $\mathbf{q}(\cdot)$, \mathbf{d}^{obs} , ℓ

for $i = 1, 2, \dots, \ell$ **do** ▷ Parallelisable

Generate $\mathbf{k}_i \sim \pi(\mathbf{k})$ ▷ Prior parameter sample

Compute $\mathbf{d}_i = \mathbf{f}(\mathbf{k}_i)$ ▷ Corresponding forward model output

Compute $\mathbf{p}_i = \mathbf{q}(\mathbf{k}_i)$ ▷ Corresponding predictive model output

end for

Compute means: $\mathbf{d}_0, \mathbf{q}_0$ ▷ Equation (9)

Compute (cross-)covariance matrices: $\Gamma_d, \Gamma_p, \Gamma_{pd}, \Gamma_{dp}$ ▷ Equation (8)

Compute conditional mean and covariance of QoIs: $\mathbf{p}_{0|\mathbf{d}^{\text{obs}}}, \Gamma_{p|\mathbf{d}^{\text{obs}}}$ ▷ Equation (10)

Generate conditional predictive samples: $\mathbf{p}^{\text{samp}}|\mathbf{d}^{\text{obs}}$ ▷ Equation (11)

3 Computational Examples

We now demonstrate the DSI approach by applying it to a simplified two-dimensional problem, as well as a large-scale, three-dimensional reservoir model. Both problems are adapted from those presented in de Beer (2024b). We first outline the governing equations for general geothermal reservoir modelling, before presenting the results of each model problem.

3.1 Governing Equations

The dynamics of a geothermal reservoir are described (mathematically) by a non-isothermal, multi-phase version of Darcy’s law, enforcing conservation of mass and energy (Croucher et al., 2020; O’Sullivan & O’Sullivan, 2016). In what follows, we denote by $\Omega \in \mathbb{R}^3$ the domain of interest, with boundary $\partial\Omega$ and outward-facing normal vector \mathbf{n} . Furthermore, we let κ denote the number of each component (e.g., water, air, energy). The governing equations, expressed in integral form, are then

$$\frac{d}{dt} \int_{\Omega} M^{\kappa} d\mathbf{x} = - \int_{\partial\Omega} \mathbf{F}^{\kappa} \cdot \mathbf{n} d\sigma + \int_{\Omega} q^{\kappa} d\mathbf{x}, \quad \kappa = 1, 2, \dots, N+1, \quad (12a)$$

where components $\kappa = 1, 2, \dots, N$ denote the mass components and component $\kappa = N+1$ denotes the energy component. For each mass component, M^{κ} denotes mass density (kg m^{-3}), \mathbf{F}^{κ} denotes mass flux ($\text{kg m}^{-2} \text{s}^{-1}$), and q^{κ} denotes mass sources or sinks ($\text{kg m}^{-3} \text{s}^{-1}$). For the energy component, M^{κ} denotes energy density (J m^{-3}), \mathbf{F}^{κ} denotes energy flux ($\text{J m}^{-2} \text{s}^{-1}$), and q^{κ} denotes energy sources or sinks ($\text{J m}^{-3} \text{s}^{-1}$). The mass and energy densities can be expressed as

$$M^{\kappa} = \begin{cases} \phi(\rho_l S_l X_l^{\kappa} + \rho_v S_v X_v^{\kappa}), & \kappa < N+1, \\ (1-\phi)\rho_r u_r T + \phi(\rho_l u_l S_l + \rho_v u_v S_v), & \kappa = N+1, \end{cases} \quad (12b)$$

where ϕ denotes porosity (dimensionless), S_l and S_v denote liquid saturation and vapour saturation (dimensionless) respectively, ρ_l , ρ_v and ρ_r denote the density of the liquid, vapour and rock (kg m^{-3}) respectively, X_l^{κ} and X_v^{κ} denote the liquid and vapour mass fractions (dimensionless) of component κ respectively, u_l and u_v denote the internal energy of the liquid and vapour (J kg^{-1}) respectively, u_r denotes the specific heat of the

rock ($\text{J kg}^{-1} \text{K}^{-1}$), and T denotes temperature (K). Next, the mass ($\kappa < N+1$) fluxes are given by the sum of the mass flux of liquid and the mass flux of vapour,

$$\mathbf{F}^\kappa = \mathbf{F}_l^\kappa + \mathbf{F}_v^\kappa, \quad \mathbf{F}_l^\kappa = -\frac{\mathbf{k}k_{rl}}{\nu_l} X_l^\kappa (\nabla p - \rho_l \mathbf{g}), \quad \mathbf{F}_v^\kappa = -\frac{\mathbf{k}k_{rv}}{\nu_v} X_v^\kappa (\nabla p - \rho_v \mathbf{g}). \quad (12c)$$

Here, \mathbf{k} represents the permeability tensor (m^2), p denotes pressure (Pa), ν_l and ν_v denote the kinematic viscosity of liquid and vapour ($\text{m}^2 \text{s}^{-1}$) respectively, k_{rl} and k_{rv} denote relative permeabilities (dimensionless), and \mathbf{g} denotes gravitational acceleration (m s^{-2}). Finally, the energy ($\kappa = N+1$) flux is given by

$$\mathbf{F}^\kappa = -K \nabla T + \sum_{m=1}^N \sum_{\chi} h_{\chi}^m \mathbf{F}_{\chi}^m, \quad (12d)$$

where h_{χ}^m denotes the specific enthalpy (J kg^{-1}) of mass component m in phase χ , and K denotes thermal conductivity ($\text{J s}^{-1} \text{m}^{-1} \text{K}^{-1}$).

3.2 Two-Dimensional Single-Phase Model

Our first model problem serves to provide a comparison between the posterior predictions produced using MCMC, linearisation about the MAP estimate, and DSI, when applied to a high-dimensional subsurface flow problem. Problems of a similar nature are often used as benchmarks when evaluating uncertainty quantification algorithms (see, e.g., Aristoff and Bangerth (2023); Christie and Blunt (2001)).

3.2.1 Problem Setup

For this problem, we make several simplifications to the governing equations introduced in Section 3.1. Namely, we consider a two-dimensional reservoir with domain $\Omega = (0 \text{ m}, 1000 \text{ m})^2$, containing single-phase, isothermal, slightly compressible fluid (see, e.g., Z. Chen (2007)), with a set of n_w production wells. We further assume that the permeability tensor, \mathbf{k} , is isotropic. In this case, Equation (12) simplifies to

$$c\phi \frac{\partial p}{\partial t} - \frac{1}{\mu} \nabla \cdot (\mathbf{k} \nabla p) = \sum_{i=1}^{n_w} q_i \delta(\mathbf{x} - \mathbf{x}_i), \quad \mathbf{x} \in \Omega, \quad t \in (0, \tau], \quad (13)$$

where c denotes fluid compressibility (assumed to be $2.9 \times 10^{-8} \text{ Pa}^{-1}$), μ denotes dynamic viscosity (assumed to be 0.5 mPa s), q_i denotes the extraction rate of well i , and $\delta(\mathbf{x} - \mathbf{x}_i)$ denotes a Dirac delta mass centred at well i , the location of which is indicated by \mathbf{x}_i . We assume a reservoir porosity of $\phi = 0.3$, and impose the boundary and initial conditions

$$\begin{aligned} -\mathbf{k} \nabla p \cdot \mathbf{n} &= 0, & \mathbf{x} \in \partial\Omega, & \quad t \in (0, \tau], \\ p &= p_0, & \mathbf{x} \in \Omega, & \quad t = 0. \end{aligned} \quad (14)$$

In the above, p_0 denotes the initial reservoir pressure, which we assume to be 20 MPa . The sole uncertain parameter is the (spatially varying, isotropic) permeability of the reservoir, k .

We consider a setup in which a set of $n_w = 9$ production wells operate over a period of $\tau = 160$ days. The location of each well is indicated in Figure 1. For the first 40 days, each of the odd-numbered wells extracts fluid at a rate of $50 \text{ m}^3 \text{ day}^{-1}$, while the even-numbered wells are turned off. For the next 40 days, this is reversed; the even-numbered wells extract fluid at a rate of $50 \text{ m}^3 \text{ day}^{-1}$, while the odd-numbered wells are turned off. For the next 40 days, all wells are turned off, before operating at a rate of $25 \text{ m}^3 \text{ day}^{-1}$ for the final 40 days. Figure 2 shows the true reservoir pressure at the end of each 40-day period.

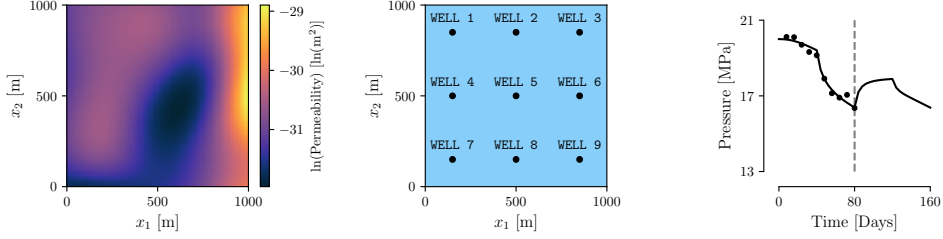


Figure 1. The setup for the simplified two-dimensional reservoir model. Left: the true log-permeability field. Centre: the locations of the production wells. Right: the pressure in well 8; the solid line denotes the true pressure, the dots denote the noisy observations, and the dashed line denotes the end of the observation period.

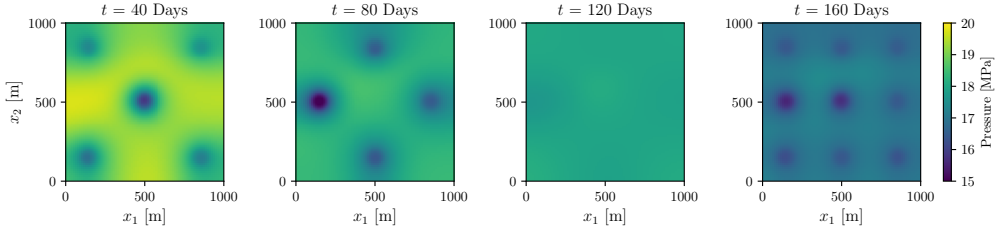


Figure 2. The true reservoir pressure at $t = 40$, $t = 80$, $t = 120$ and $t = 160$ days.

3.2.2 Prior Parametrisation

As is standard, when solving the inverse problem we work in terms of the log-permeability, $u := \ln(k)$, which ensures that the resulting estimates of the permeability are positive. We parametrise the log-permeability of the reservoir using a Gaussian random field (GRF) with a mean function of $m(\mathbf{x}) = -31 \ln(\text{m}^2)$, and a squared-exponential covariance function (Williams & Rasmussen, 2006), given by

$$\mathcal{C}(\mathbf{x}, \mathbf{x}') = \sigma^2 \exp \left(-\frac{1}{2l^2} \|\mathbf{x} - \mathbf{x}'\|^2 \right). \quad (15)$$

We use a standard deviation of $\sigma = 0.75 \ln(\text{m}^2)$ and a characteristic lengthscale of $l = 250 \text{ m}$. To reduce the dimension of the parameter space and accelerate the convergence of our MCMC sampler, we approximate this GRF using a truncated Karhunen–Loève expansion; that is,

$$\mathbf{u} \approx \sum_{i=1}^n \sqrt{\lambda_i} \mathbf{v}_i \xi_i, \quad (16)$$

where $\xi_i \sim \mathcal{N}(0, 1)$. In Equation (16), $\{(\lambda_i, \mathbf{v}_i)\}_{i=1}^n$ denote the n largest eigenpairs of the covariance matrix of the (discretised) GRF, where n is typically small compared to the dimension of the field. Under this parametrisation, the values of the coefficients $\{\xi_i\}_{i=1}^n$ become the targets of inference. Here, we retain $n = 50$ coefficients. Figure 3 shows several draws from the prior.

3.2.3 Data

We assume that the pressure at each well is recorded every 8 days for the first half of the production period; this gives a total of 90 measurements. We add independent Gaussian noise with a standard deviation of 1% of the initial reservoir pressure to each observation. Figure 1 shows the data collected at well 8.

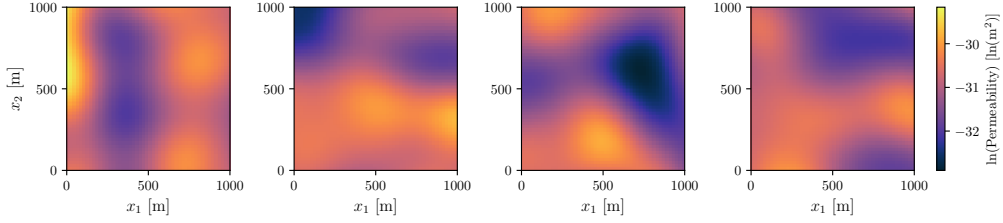


Figure 3. Samples from the prior distribution of the reservoir permeability.

3.2.4 Simulation

We discretise the system using a cell-centred finite difference scheme (Z. Chen, 2007; Haber & Hanson, 2007), and use the backward Euler method to solve for the dynamics of the system over time. The permeability distribution of the true system, shown in Figure 1, is generated using a draw from the prior. To avoid the “inverse crime” of generating the synthetic data and solving the inverse problem using the same numerical discretisation (Kaipio & Somersalo, 2006, 2007), we use an 80×80 grid when simulating the dynamics of the true system, but a 50×50 grid when carrying out each inversion.

3.2.5 Inference Methods

We aim to use the data collected at each well over the first half of the production period to estimate the pressure at each well over the entire period.

We compute a complete characterisation of the posterior and posterior predictive distributions using the preconditioned Crank-Nicolson MCMC sampler (V. Chen et al., 2019; Cotter et al., 2013), which is commonly used to solve high-dimensional inverse problems. We run four Markov chains, each initialised at a random draw from the prior, for 500,000 iterations, and discard the first half of each chain as burn in. These results provide a reference to which we can compare the posterior predictive distributions produced using linearisation about the MAP estimate and data space inversion.

To compute the MAP estimate, we use a matrix-free inexact Gauss-Newton conjugate gradient method (see, e.g., Haber and Hanson (2007); Petra and Stadler (2011)). The process of computing the MAP estimate and forming the approximate posterior covariance matrix requires 244 “forward-like” solves (these include both forward and adjoint solves, which are associated with similar computational costs), though this could, of course, be reduced through the use of an improved optimisation method.

When approximating the posterior predictive distribution using DSI, we use an initial set of 1000 samples from the prior to estimate the conditional mean and covariance of the predictive quantities of interest using the methodology outlined in Section 2.5. We then examine the differences in the results when the number of samples used is varied.

3.2.6 Results

Figure 4 shows a set of 1000 samples of the pressure at wells 1, 6 and 8, drawn from the posterior predictive distributions produced using MCMC, linearisation about the MAP estimate, and DSI. In all cases, a set of 1000 samples from the prior are also presented for comparison. We observe that, in all cases, the posterior uncertainty is significantly reduced in comparison to the prior uncertainty, and the true pressure at each well is contained within the predictions. The predictions generated using linearisation about the MAP estimate appear very similar to those generated using MCMC. By contrast, the predictions generated using DSI tend to have slightly greater variance, particularly in

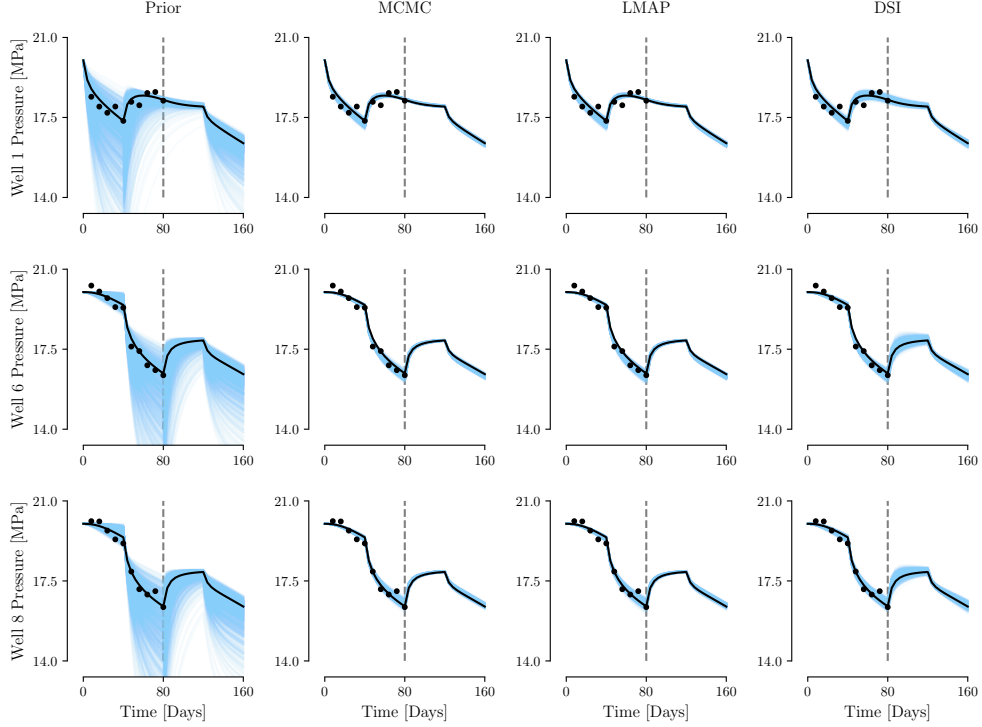


Figure 4. Samples from the prior predictive distribution (left) and the posterior predictive distributions generated using MCMC (centre left), linearisation about the MAP estimate (centre right), and DSI (right), for wells 1, 6 and 8. In all plots, the blue lines indicates the samples, the black line denotes the true well pressure, the black dots denote the observations, and the dashed grey line denotes the end of the data collection period.

the second half of the production period. Nonetheless, these predictions show a significant reduction in uncertainty in comparison to the prior and tend to assign high probability to the pressure of the true system. Figure 5 shows the estimates of the marginal densities of the pressure in each well at the end of the production period ($t = 160$ days) obtained using each method (we note that the DSI densities are known analytically); these plots largely reinforce these conclusions.

Figure 6 shows how the posterior predictions change as the number of samples used to estimate the covariance matrices in Equation (8) varies. The posterior predictive distribution generated using 10 samples is often significantly different to the approximations generated using larger numbers of samples (see, e.g., well 2 and well 3). However, after the number of samples reaches 100, the predictive distributions begin to look very similar to one another; this suggests that 100 samples is an appropriate number to use when applying DSI to this model problem. We note, however, that there is no guarantee we will observe similar results when applying DSI to other problems.

3.3 Three-Dimensional Reservoir Model

The second test case we consider is a synthetic three-dimensional reservoir model.

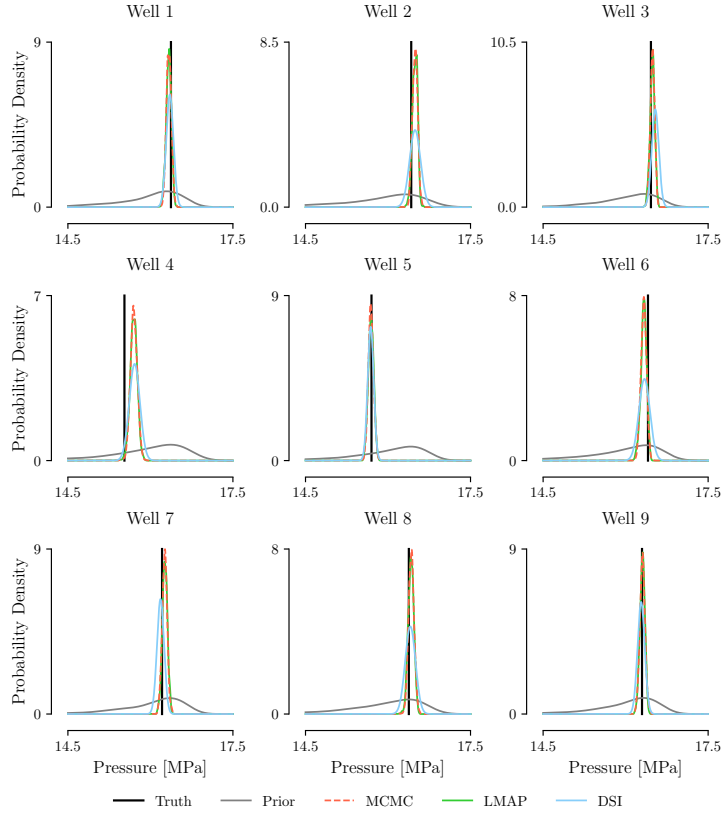


Figure 5. The prior predictive distribution (grey) and posterior predictive distributions of the pressure in each well at the end of the production period ($t = 160$ days) obtained using MCMC (orange), linearisation about the MAP estimate (green), and DSI (blue). The black line in each plot denotes the true pressure.

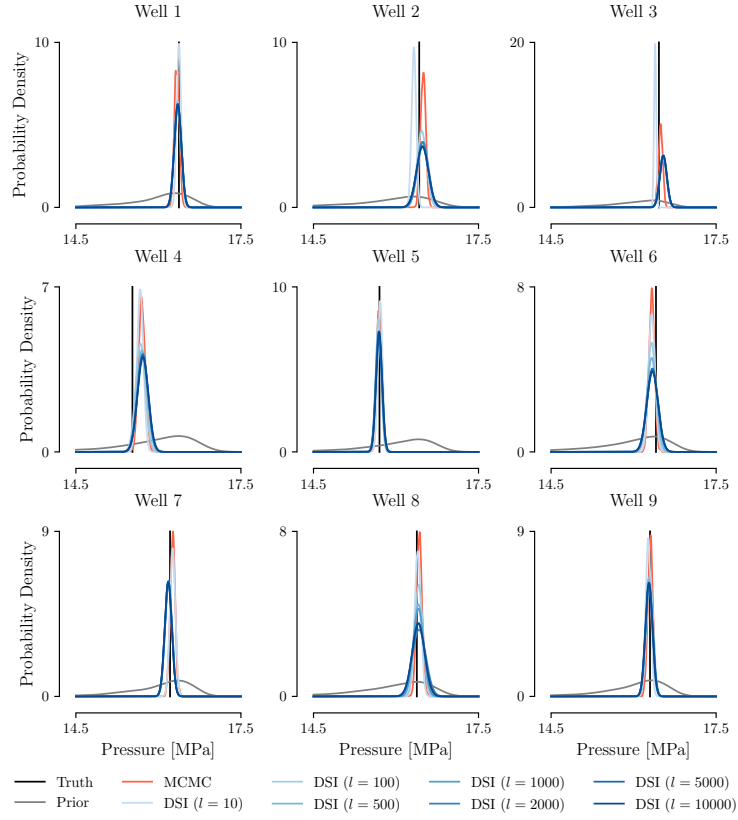


Figure 6. The prior predictive distribution (grey) and posterior predictive distributions of the pressure in each well at the end of the production period ($t = 160$ days) obtained using MCMC (orange), and DSI with varying numbers of samples (blue). The black line in each plot denotes the true pressure.

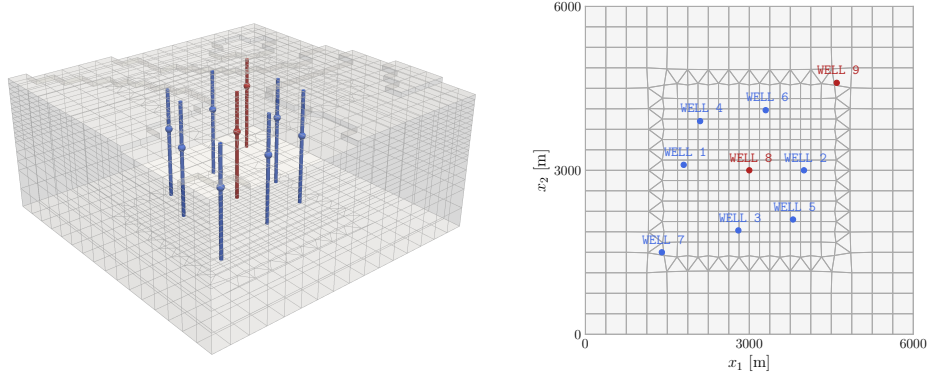


Figure 7. The mesh of the synthetic reservoir model, and the locations of each production well. Existing wells are denoted using blue and new wells are denoted using red.

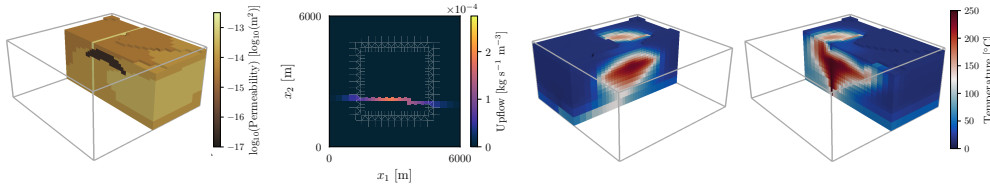


Figure 8. The true permeability structure (first plot), mass upflows (second plot) and natural state convective plume (third and fourth plots) of the synthetic reservoir model.

3.3.1 Problem Setup

The model domain, shown in Figure 7, spans 6000 m in the horizontal (x_1 and x_2) directions, and extends to a depth of 3000 m in the vertical direction. Figure 8 shows the true subsurface permeability structure, mass upflows, and natural state convective plume of the system.

We assume that we have been extracting fluid at each of the seven existing wells (wells 1–7 in Figure 7) of the system at a rate of 0.25 kg s^{-1} over a period of one year. We then wish to estimate the downhole temperature profiles associated with each of the existing wells, as well as two new wells (well 8 and well 9 in Figure 7), and to predict how the pressure and enthalpy of the fluid extracted at each well will change if we operate all wells at the increased rate of 0.5 kg s^{-1} for a further year. Each well has a single feedzone at a depth of 1200 m. As is standard in geothermal reservoir modelling, we consider a combined natural state and production history simulation (O’Sullivan & O’Sullivan, 2016); that is, we simulate the dynamics of the system until steady-state conditions are reached, then use the resulting state of the system as the initial condition for the subsequent production simulation.

3.3.2 Prior Parametrisation

When parametrising the prior, we consider uncertainty in both the subsurface permeability structure (modelled as isotropic, for simplicity) and the location and magnitude of the hot mass upflow at the base of the reservoir. All other reservoir properties are assumed known. The rock of the reservoir is assumed to have a porosity of 0.1, a density of 2500 kg m^{-3} , a thermal conductivity of $2.5 \text{ W m}^{-1} \text{ K}^{-1}$, and a specific heat of $1000 \text{ J kg}^{-1} \text{ K}^{-1}$.

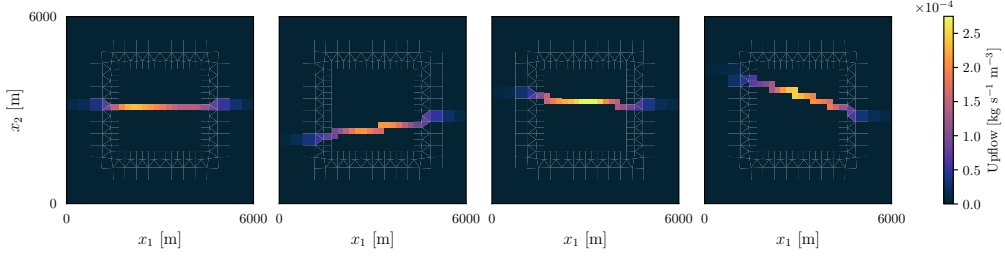


Figure 9. Mass upflows sampled from the prior.

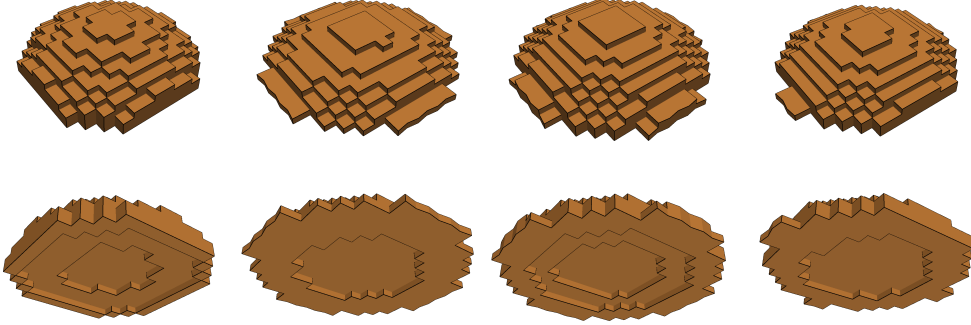


Figure 10. The top surfaces (top row) and bottom surfaces (bottom row) of clay cap geometries sampled from the prior.

The top boundary of the model is set to a constant pressure of 1 bar and a temperature of 20°C; this represents an atmospheric boundary condition. The side boundaries are closed. We impose a background heat flux of 200 mW m^{-2} through all cells on the bottom boundary except for those which are associated with a mass upflow. All of the mass upflow entering through the bottom boundary is associated with an enthalpy of 1500 kJ kg^{-1} .

We assume that there is a single linear, vertical fault running through the reservoir from east to west. However, we treat the exact location of the fault, as well as the magnitude of the mass upflow contained within it, as unknown. We assume that the points at which the fault intersects the eastern and western boundaries of the model domain are independent and uniformly distributed between 1500 m and 4500 m, and that the upflow within each cell along the fault is modelled using a Gaussian random field with a squared-exponential covariance function (see Eq. (15)) and a mean and standard deviation that reduce as the horizontal distance to the centre of the model domain increases, reflecting a prior belief that the upflow tends to be greatest near the centre of the model domain. The parameters of this GRF are chosen such that the total mass upflow entering the model domain tends to be between 80 kg s^{-1} and 120 kg s^{-1} . Figure 9 shows several samples of mass upflows drawn from the prior.

To parametrise the permeability structure of the reservoir, we first partition the domain of the model into three regions with variable interfaces: the fault (which has a high permeability), a low-permeability clay cap, and a moderately permeable background region. We model the clay cap as the deformation of a star-shaped set, with a boundary represented using a truncated Fourier series with uncertain coefficients. Figure 10 shows several clay cap geometries drawn from the prior; for a complete description of this parametrisation, the reader is referred to de Beer (2024b). Where the clay cap and fault intersect, the clay cap takes priority.

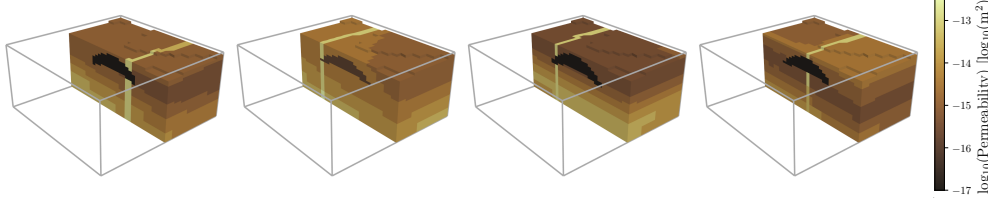


Figure 11. Permeability structures sampled from the prior.

To model the permeability within each region, we use the level set method (Iglesias et al., 2016), which is often used in the modelling of subsurface systems to generate distinct regions with common geophysical characteristics (see, e.g., Muir and Tsai (2020); Tso et al. (2021)). These regions are defined using the contours of a continuous function, referred to as the level set function, which we denote using $\varphi(\cdot)$. In each region, we first specify a set of rock types with varying permeabilities, then select a set of constants to threshold the level set function at to produce each rock type. For instance, the permeability within the fault region is given by

$$k(\mathbf{x}) = \begin{cases} 10^{-13.5} \text{ m}^2, & \varphi(\mathbf{x}) < -0.5, \\ 10^{-13.0} \text{ m}^2, & -0.5 \leq \varphi(\mathbf{x}) < 0.5, \\ 10^{-12.5} \text{ m}^2, & 0.5 \leq \varphi(\mathbf{x}). \end{cases} \quad (17)$$

The permeability of each of the other regions is defined similarly. We allow the permeability of the clay cap to vary between 10^{-17} m^2 and 10^{-16} m^2 , and the permeability of the background region to vary between $10^{-15.5} \text{ m}^2$ and $10^{-13.5} \text{ m}^2$. In all regions, we choose the level set function to be a centred GRF with a squared-exponential covariance function, with a standard deviation chosen such that the prior probabilities of a given location within each region belonging to each rock type are approximately equal. The lengthscale of each level set function in the horizontal (x_1 and x_2 directions) is 8000 m, while the lengthscale in the vertical (x_3) direction is 2000 m. This tends to result in the generation of layered structures. Figure 11 shows several permeability structures sampled from the prior.

3.3.3 Data

We assume that we have access to measurements of the natural state temperature at seven equispaced points down each of wells 1–7, as well as measurements of the pressure and enthalpy of the fluid extracted from each well at three-month intervals over the first year of the production period. This gives a total of 119 measurements. We add independent Gaussian noise to each measurement, with a standard deviation equal to 2% of the maximum value of the corresponding data type. Figure 12 shows the data collected at well 1. No data is collected at well 8 or well 9.

3.3.4 Simulation

All simulations are carried out using the open-source simulator Waiwera (Croucher et al., 2020), which uses a finite volume discretisation of the governing equations in Section 3.1, and are run in parallel on a high-performance computing cluster provided by New Zealand eScience Infrastructure. As in our previous model problem, to avoid the “inverse crime” of generating the synthetic data and solving the inverse problem using the same numerical discretisation (Kaipio & Somersalo, 2006, 2007), we use a mesh comprised of 13,383 cells when simulating the dynamics of the true system (generated using a draw from the prior), but a mesh comprised of 8,788 cells (plotted in Figure 7) when

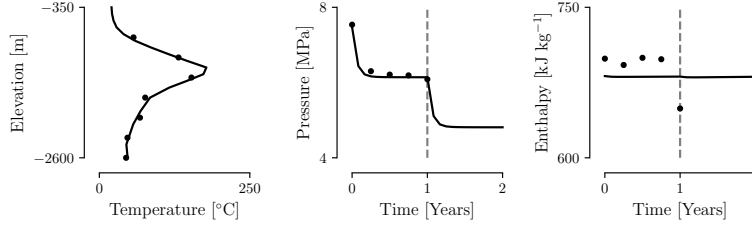


Figure 12. The natural state downhole temperature data (left), transient pressure data (centre) and transient enthalpy data (right) collected at well 1. In all plots, the solid line denotes the true reservoir state and the dots denote noisy observations. In the pressure and enthalpy plots, the dashed grey line denotes the end of the data collection period.

carrying out the simulations required to approximate the posterior predictive distribution using DSI.

For the DSI algorithm, we run 1000 simulations using sets of parameters drawn from the prior. As is common in geothermal reservoir modelling, some of these converge to physically unreasonable values (for example, the reservoir pressure reduces below atmospheric pressure), while others do not converge entirely. After discarding these, we are left with 676 simulations which are used to estimate the conditional mean and covariance of the predictive quantities of interest.

3.3.5 Results

Figure 13 shows samples from the prior predictive distribution, and the approximation to the posterior predictive distribution obtained using DSI, for the downhole temperature profiles at the end of the data collection period, and the transient feedzone pressure and enthalpy, in well 3 and well 4. Results for other wells at which data is collected are similar. In all cases, applying the DSI algorithm gives a significant reduction in uncertainty, and the state of the true system generally has high posterior probability. As expected, the uncertainty in the pressure of each feedzone increases after the end of the data collection period. However, the uncertainty in the enthalpy of each feedzone remains fairly similar throughout the whole production period; this is because in all prior simulations the enthalpy tends to change very little from its natural state value.

Figure 14 shows samples of the same quantities as Figure 13, but for well 8 and well 9, at which no data is collected. In both cases, the uncertainty in each predictive quantity of interest is reduced after applying the DSI algorithm, and the state of the true system has high posterior probability. However, this reduction in uncertainty is significantly less than for well 3 and well 4; this is expected, given that we do not have access to any direct information on the state of the reservoir down these wells.

We note that some of the posterior predictions generated using the DSI algorithm do not appear to be physically realistic. Perhaps the most obvious example of this is the predictions of the feedzone pressure in well 8; in a significant number of draws from the posterior predictive distribution generated using DSI, the pressure increases significantly at the end of the first year of the production period, despite this being the time at which the well begins to extract fluid from the system. This is likely a result of the fact that the DSI algorithm does not use the physical model when approximating the posterior predictive distribution; increases of this magnitude are not observed in any of the prior simulations. It is, however, possible to enforce physical constraints on the characteris-

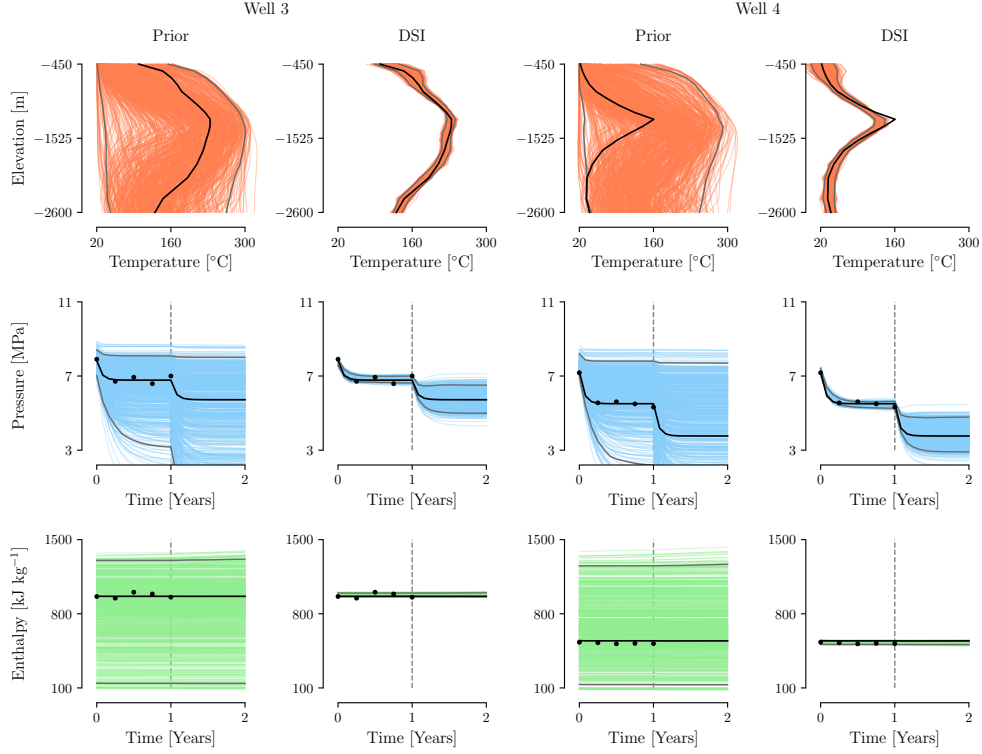


Figure 13. The downhole temperatures at the end of the data collection period (red), and the transient feedzone pressure (blue) and enthalpy (green), in well 3 (first and second columns) and well 4 (third and fourth columns). For both wells, samples from the prior predictive distribution and the approximation to the posterior predictive distribution computed using DSI are shown. In all plots, the black line denotes the true reservoir state and the grey lines indicate the central 95% of the samples. In the pressure and enthalpy plots, the black dots denote the noisy observations and the dashed grey line denotes the end of the data collection period.

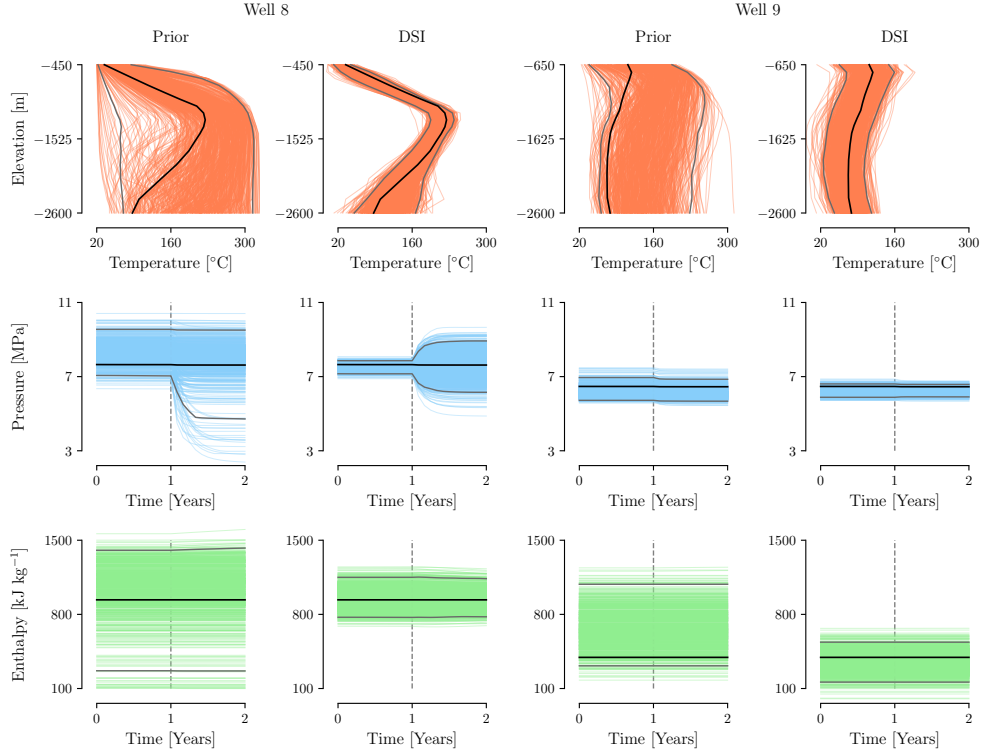


Figure 14. The downhole temperatures at the end of the data collection period (red), and the transient feedzone pressure (blue) and enthalpy (green), in well 8 (first and second columns) and well 9 (third and fourth columns). For both wells, samples from the prior predictive distribution and the approximation to the posterior predictive distribution computed using DSI are shown. In all plots, the black line denotes the true reservoir state and the grey lines indicate the central 95% of the samples.

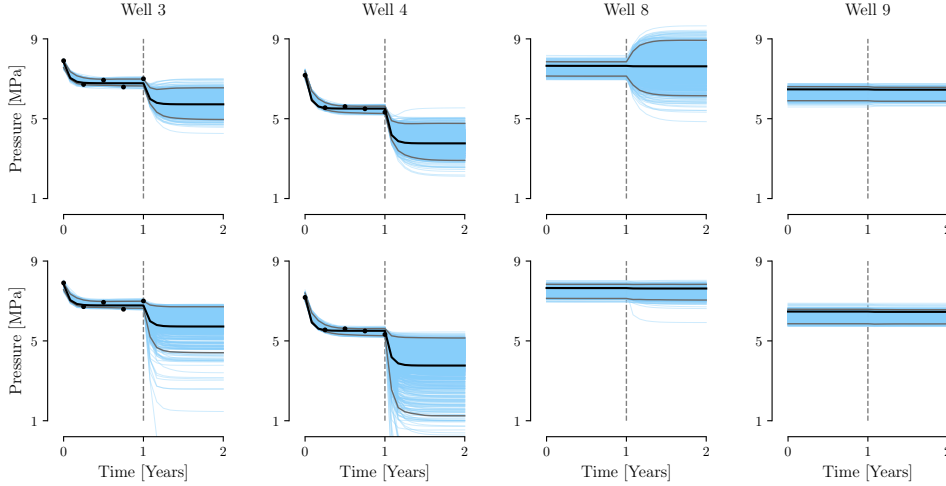


Figure 15. Samples from the approximation to the posterior predictive distribution of the feedzone pressure in wells 3, 4, 8, and 9 using DSI without any transformations applied (top row) and DSI with a transformation applied that imposes a limit on the increase in pressure between successive timesteps (bottom row). In all plots, the blue lines indicate the samples, the grey lines denote the central 95% of the samples, the black line denotes the true feedzone pressure, the black dots denote the observations, and the dashed grey line denotes the end of the observation period.

tics of the posterior predictive distribution generated using DSI through the use of suitable transformations; we illustrate one possible transformation here, though this is by no means the best possible choice. To limit the increase in pressure after the first year of production, we first specify a maximum possible increase, δ , in the feedzone pressure between two successive timesteps (we select this such that it is an upper bound on the increases in the pressure observed in the prior simulations to ensure that the resulting transformation is well-defined). We then replace the modelled pressure at each timestep after the end of the observation period with the difference between the pressure at the current timestep and the previous pressure; that is, $\Delta p^{(t)} := p^{(t)} - p^{(t-1)}$. Next, we apply the transformation

$$\Delta p^{(t)} \mapsto \ln(-\Delta p^{(t)} + \delta) \quad (18)$$

to each of these differences. Finally, we apply DSI to approximate the posterior predictive distribution of the transformed pressure differences. Then, after sampling from this distribution, we can apply the inverse of the transformation in Equation (18) to obtain the corresponding pressures. Carrying out the DSI procedure in the transformed space ensures that none of the changes in pressure between two successive timesteps drawn from the posterior predictive distribution exceed δ .

Figure 15 shows the posterior predictions of the pressure in wells 3, 4, 8, and 9 obtained using DSI with and without the aforementioned transformation applied using $\delta = 0.01$ MPa (note that we record the reservoir state at one-month intervals throughout the production period). With the exception of well 9, the use of the transformation results in substantive changes to the posterior predictions. There are no longer any predictions in which the feedzone pressure increases significantly, which aligns with our physical intuition. We note, however, that without knowledge of the true posterior predictive distribution, we cannot confirm whether the use of this transformation improves the resulting approximation to the posterior predictive distribution.

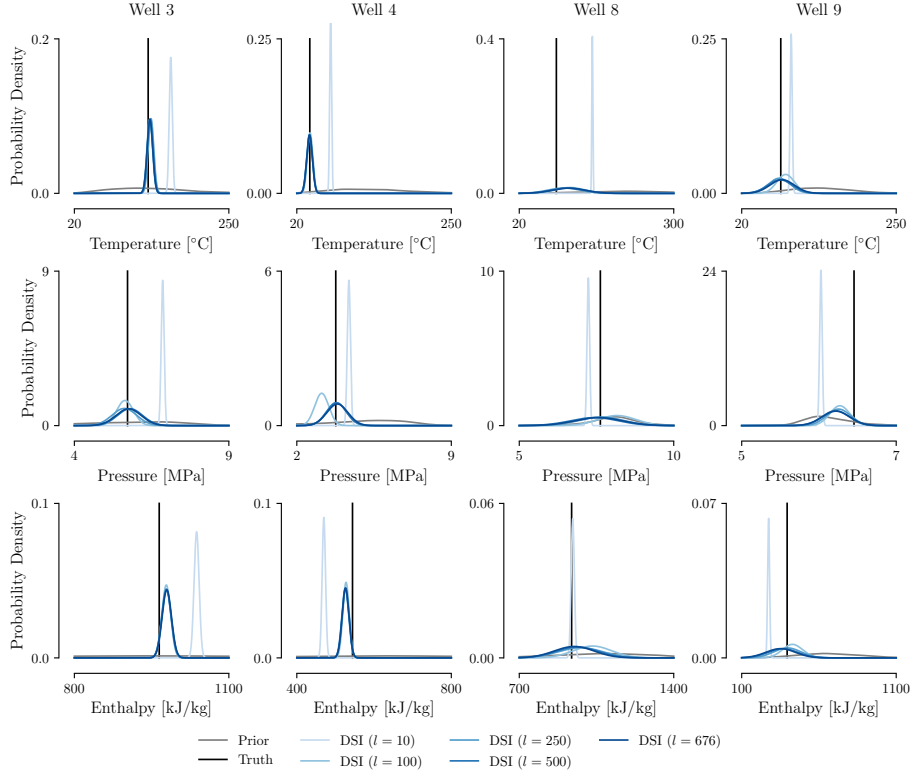


Figure 16. The prior predictive distribution (grey) and posterior predictive distributions of the temperature at the bottom of the well at the end of the data collection period, and the feed-zone pressure and enthalpy at the end of the production period, for wells 3, 4, 7 and 8. The black line in each plot denotes the true reservoir state.

Finally, Figure 16 shows how the posterior predictive distributions for the temperature at the bottom of the well at the end of the data collection period and the feedzone pressure and enthalpy at the end of the production period change as the number of samples used to estimate the covariance matrices in Equation (8) varies, for wells 3, 4, 7 and 8. Here, no transformations are applied. As in the two-dimensional setting, we observe that, when 10 samples are used, the resulting estimates are significantly different to those obtained using a greater number of samples. Additionally, they often fail to capture the truth with non-negligible probability. When 100 samples are used, the resulting estimates appear to be fairly consistent with those obtained using larger sample sizes (with the exception of the pressure in well 4), and when sample sizes of more than 250 are used there appears to be very little difference in the results.

4 Conclusions and Outlook

We have demonstrated that the data space inversion methodology provides an efficient, derivative-free means of making geothermal reservoir model predictions, with quantified uncertainty, conditioned on observed data. We have also illustrated how the approximation to the posterior predictive distribution generated using DSI changes as the number of samples from the prior that are used as part of the algorithm is varied, and how the use of suitable reparametrisations can improve this approximation.

An obvious next step will be to demonstrate the application of the DSI methodology to a real-world case study arising in geothermal reservoir modelling. A model of a real-world geothermal system is likely to require a more complex prior than we have used in our model problems; the prior will need to account for the full, anisotropic permeability structure of the reservoir, as well as additional uncertain parameters such as the reservoir porosity. There may also be additional data to consider, such as CO₂ fractions or information on surface features. However, we anticipate that the application of the DSI framework will remain much the same.

There are a variety of extensions of the DSI framework that would be valuable to explore in a geothermal setting. In particular, DSI is likely to be well-suited to solving goal-oriented optimal experimental design problems, in which one is interested in identifying a data collection plan that minimises a measure of the expected posterior uncertainty in the predictive quantities of interest. Solving a goal-oriented OED problem generally requires the repeated computation of the posterior predictive distribution associated with the possible data one could expect to collect; because the DSI framework uses the same set of simulations from the prior when approximating the posterior predictive distribution, regardless of the data collected, solving the OED problem would require no more reservoir model simulations than solving a single inverse problem. For similar ideas within the context of the Bayesian evidential learning framework, see Thibaut et al. (2021). Another potential area of interest is optimal control; for example, Jiang et al. (2020) describe an extension of the DSI framework to optimise the management of oil reservoirs, by treating user-specified well controls as “data” to be conditioned on later, which allows for the efficient approximation of the posterior predictive distribution under various management scenarios.

Overall, our findings support the idea that DSI is a useful framework for uncertainty quantification in geothermal reservoir modelling, and should be investigated further.

Open Research Section

The code and models used to carry out the experiments and generate the figures in this paper are archived on Zenodo (de Beer, 2024a), and are also available on GitHub (<https://github.com/alexgdebeer/GeothermalDSI>) under the MIT license.

Acknowledgments

The authors wish to acknowledge the use of New Zealand eScience Infrastructure (NeSI; www.nesi.org.nz) high performance computing facilities as part of this research. These facilities are funded jointly by NeSI’s collaborator institutions and through the Ministry of Business, Innovation & Employment’s Research Infrastructure programme. The authors would like to thank the MBIE research programme “Empowering Geothermal” which has in part funded this research. Finally, the authors wish to thank John Doherty for several fruitful discussions on the data space inversion methodology.

References

- Aristoff, D., & Bangerth, W. (2023). A benchmark for the Bayesian inversion of coefficients in partial differential equations. *SIAM Review*, 65(4), 1074–1105. doi: <https://doi.org/10.1137/21M1399464>
- Athens, N. D., & Caers, J. K. (2019). A Monte Carlo-based framework for assessing the value of information and development risk in geothermal exploration. *Applied Energy*, 256, 113932. doi: <https://doi.org/10.1016/j.apenergy.2019.113932>
- Békési, E., Struijk, M., Bonté, D., Veldkamp, H., Limberger, J., Fokker, P. A., . . . van Wees, J.-D. (2020). An updated geothermal model of the Dutch subsur-

- face based on inversion of temperature data. *Geothermics*, 88, 101880. doi: <https://doi.org/10.1016/j.geothermics.2020.101880>
- Bjarkason, E. K., Maclaren, O. J., Nicholson, R., Yeh, A., & O'Sullivan, M. J. (2020). Uncertainty quantification of highly-parameterized geothermal reservoir models using ensemble-based methods. In *Proc. World Geothermal Congress*. Retrieved from <https://hdl.handle.net/2292/65029>
- Bjarkason, E. K., Maclaren, O. J., O'Sullivan, J. P., & O'Sullivan, M. J. (2018). Randomized truncated SVD Levenberg-Marquardt approach to geothermal natural state and history matching. *Water Resources Research*, 54(3), 2376–2404. doi: <https://doi.org/10.1002/2017WR021870>
- Bjarkason, E. K., O'Sullivan, J. P., Yeh, A., & O'Sullivan, M. J. (2019). Inverse modeling of the natural state of geothermal reservoirs using adjoint and direct methods. *Geothermics*, 78, 85–100. doi: <https://doi.org/10.1016/j.geothermics.2018.10.001>
- Calvetti, D., & Somersalo, E. (2007). *An introduction to Bayesian scientific computing: ten lectures on subjective computing*. Springer New York. doi: <https://doi.org/10.1007/978-0-387-73394-4>
- Chen, V., Dunlop, M. M., Papaspiliopoulos, O., & Stuart, A. M. (2019). *Dimension-robust MCMC in Bayesian inverse problems*.
- Chen, Y., & Oliver, D. S. (2013). Levenberg–Marquardt forms of the iterative ensemble smoother for efficient history matching and uncertainty quantification. *Computational Geosciences*, 17, 689–703. doi: <https://doi.org/10.1007/s10596-013-9351-5>
- Chen, Z. (2007). *Reservoir simulation: mathematical techniques in oil recovery*. SIAM. doi: <https://doi.org/10.1137/1.9780898717075>
- Christie, M. A., & Blunt, M. J. (2001). Tenth SPE comparative solution project: A comparison of upscaling techniques. *SPE Reservoir Evaluation & Engineering*, 4(04), 308–317. doi: <https://doi.org/10.2118/72469-PA>
- Cotter, S. L., Roberts, G. O., Stuart, A. M., & White, D. (2013). MCMC methods for functions: modifying old algorithms to make them faster. *Statistical Science*, 28, 424–446. doi: <https://doi.org/10.1214/13-STS421>
- Croucher, A., O'Sullivan, M., O'Sullivan, J., Yeh, A., Burnell, J., & Kissling, W. (2020). Waiwera: A parallel open-source geothermal flow simulator. *Computers & Geosciences*, 141, 104529. doi: <https://doi.org/10.1016/j.cageo.2020.104529>
- Cui, T., Fox, C., & O'Sullivan, M. J. (2011). Bayesian calibration of a large-scale geothermal reservoir model by a new adaptive delayed acceptance Metropolis Hastings algorithm. *Water Resources Research*, 47(10). doi: <https://doi.org/10.1029/2010WR010352>
- Cui, T., Fox, C., & O'Sullivan, M. J. (2019). A posteriori stochastic correction of reduced models in delayed-acceptance MCMC, with application to multiphase subsurface inverse problems. *International Journal for Numerical Methods in Engineering*, 118(10), 578–605. doi: <https://doi.org/10.1002/nme.6028>
- de Beer, A. (2024a). *alexgdebeer/GeothermalDSL*. (Software) doi: <https://doi.org/10.5281/zenodo.12193947>
- de Beer, A. (2024b). *Ensemble methods for geothermal inverse problems* (Master's thesis, University of Auckland). Retrieved from <https://hdl.handle.net/2292/68150>
- Delottier, H., Doherty, J., & Brunner, P. (2023). Data space inversion for efficient uncertainty quantification using an integrated surface and subsurface hydrologic model. *Geoscientific Model Development Discussions*, 2023, 1–30. doi: <https://doi.org/10.5194/gmd-16-4213-2023>
- Emerick, A. A., & Reynolds, A. C. (2013). Ensemble smoother with multiple data assimilation. *Computers & Geosciences*, 55, 3–15. doi: <https://doi.org/10.1016/j.cageo.2012.03.011>

- Gonzalez-Gutierrez, B., Sung, S., Nicholson, R., O'Sullivan, J. P., O'Sullivan, M. J., & Maclaren, O. (2018). Accelerating the solution of geothermal inverse problems using adjoint methods in Waiwera: A progress report. In *Proc. 40th New Zealand geothermal workshop*.
- Haber, E., & Hanson, L. (2007). *Model problems in PDE-constrained optimization* (Tech. Rep.). Atlanta, Georgia: Emory University.
- Hermans, T., Nguyen, F., Klepikova, M., Dassargues, A., & Caers, J. (2018). Uncertainty quantification of medium-term heat storage from short-term geophysical experiments using Bayesian evidential learning. *Water Resources Research*, 54(4), 2931–2948. doi: <https://doi.org/10.1002/2017WR022135>
- Iglesias, M. A., Law, K. J., & Stuart, A. M. (2013). Ensemble Kalman methods for inverse problems. *Inverse Problems*, 29(4), 045001. doi: <https://doi.org/10.1088/0266-5611/29/4/045001>
- Iglesias, M. A., Lu, Y., & Stuart, A. M. (2016). A Bayesian level set method for geometric inverse problems. *Interfaces and Free Boundaries*, 18(2), 181–217. doi: <https://doi.org/10.4171/IFB/362>
- Jiang, S., & Durlafsky, L. J. (2021). Treatment of model error in subsurface flow history matching using a data-space method. *Journal of Hydrology*, 603, 127063. doi: <https://doi.org/10.1016/j.jhydrol.2021.127063>
- Jiang, S., Hui, M.-H., & Durlafsky, L. J. (2021). Data-space inversion with a recurrent autoencoder for naturally fractured systems. *Frontiers in Applied Mathematics and Statistics*, 7, 686754. doi: <https://doi.org/10.3389/fams.2021.686754>
- Jiang, S., Sun, W., & Durlafsky, L. J. (2020). A data-space inversion procedure for well control optimization and closed-loop reservoir management. *Computational Geosciences*, 24, 361–379. doi: <https://doi.org/10.1007/s10596-019-09853-4>
- Kaipio, J., & Somersalo, E. (2006). *Statistical and computational inverse problems*. Springer New York. doi: <https://doi.org/10.1007/b138659>
- Kaipio, J., & Somersalo, E. (2007). Statistical inverse problems: Discretization, model reduction and inverse crimes. *Journal of Computational and Applied Mathematics*, 198(2), 493–504. doi: <https://doi.org/10.1016/j.cam.2005.09.027>
- Kitanidis, P. K. (1995). Quasi-linear geostatistical theory for inversing. *Water Resources Research*, 31(10), 2411–2419. doi: <https://doi.org/10.1029/95WR01945>
- Lima, M. M., Emerick, A. A., & Ortiz, C. E. (2020). Data-space inversion with ensemble smoother. *Computational Geosciences*, 24, 1179–1200. doi: <https://doi.org/10.1007/s10596-020-09933-w>
- Liu, D., Rao, X., Zhao, H., Xu, Y.-F., & Gong, R.-X. (2021). An improved data space inversion method to predict reservoir state fields via observed production data. *Petroleum Science*, 18(4), 1127–1142. doi: <https://doi.org/10.1016/j.petsci.2021.07.008>
- Maclaren, O. J., Nicholson, R., Bjarkason, E. K., O'Sullivan, J. P., & O'Sullivan, M. J. (2020). Incorporating posterior-informed approximation errors into a hierarchical framework to facilitate out-of-the-box MCMC sampling for geothermal inverse problems and uncertainty quantification. *Water Resources Research*, 56(1), e2018WR024240. doi: <https://doi.org/10.1029/2018WR024240>
- Manewell, N., Doherty, J., & Hayes, P. (2024). Translating pumping test data into groundwater model parameters: a workflow to reveal aquifer heterogeneities and implications in regional model parameterization. *Frontiers in Water*, 5, 1334022. doi: <https://doi.org/10.3389/frwa.2023.1334022>
- Michel, H., Nguyen, F., Kremer, T., Elen, A., & Hermans, T. (2020). 1D geological imaging of the subsurface from geophysical data with Bayesian Evidential Learning. *Computers & Geosciences*, 138, 104456. doi: <https://doi.org/10.1016/j.cageo.2020.104456>

- <https://doi.org/10.1016/j.cageo.2020.104456>
- Muir, J. B., & Tsai, V. C. (2020). Geometric and level set tomography using ensemble Kalman inversion. *Geophysical Journal International*, 220(2), 967–980. doi: <https://doi.org/10.1093/gji/ggz472>
- Oliver, D. S., He, N., & Reynolds, A. C. (1996). Conditioning permeability fields to pressure data. In *Proc. 5th European conference on the mathematics of oil recovery*.
- Omagbon, J., Doherty, J., Yeh, A., Colina, R., O’Sullivan, J., McDowell, J., . . . O’Sullivan, M. (2021). Case studies of predictive uncertainty quantification for geothermal models. *Geothermics*, 97, 102263. doi: <https://doi.org/10.1016/j.geothermics.2021.102263>
- O’Sullivan, M. J., & O’Sullivan, J. P. (2016). Reservoir modeling and simulation for geothermal resource characterization and evaluation. In *Geothermal power generation* (pp. 165–199). Elsevier. doi: <https://doi.org/10.1016/B978-0-08-100337-4.00007-3>
- O’Sullivan, J., Croucher, A., Yeh, A., & O’Sullivan, M. (2013). Improved convergence for air-water and CO₂-water TOUGH2 simulations. In *Proc. 35th New Zealand geothermal workshop*.
- Petra, N., & Stadler, G. (2011). *Model variational inverse problems governed by partial differential equations* (Tech. Rep.). Austin, Texas: Institute for Computational Engineering and Sciences, University of Texas at Austin.
- Power, A., Wong, D., Dekkers, K., Gravatt, M., Maclaren, O. J., O’Sullivan, J. P., . . . Nicholson, R. (2022). Data-space inversion for efficient geothermal reservoir model predictions and uncertainty quantification. In *Proc. 43rd New Zealand geothermal workshop*.
- Pradhan, A., & Mukerji, T. (2020). Seismic Bayesian evidential learning: Estimation and uncertainty quantification of sub-resolution reservoir properties. *Computational Geosciences*, 24(3), 1121–1140. doi: <https://doi.org/10.1007/s10596-019-09929-1>
- Scheidt, C., Li, L., & Caers, J. (2018). *Quantifying uncertainty in subsurface systems*. John Wiley & Sons. doi: <https://doi.org/10.1002/9781119325888>
- Scott, S. W., O’Sullivan, J. P., Maclaren, O. J., Nicholson, R., Covell, C., Newson, J., & Gudjónsdóttir, M. S. (2022). Bayesian calibration of a natural state geothermal reservoir model, Krafla, North Iceland. *Water Resources Research*, 58(2), e2021WR031254. doi: <https://doi.org/10.1029/2021WR031254>
- Sun, W., & Durlofsky, L. J. (2017). A new data-space inversion procedure for efficient uncertainty quantification in subsurface flow problems. *Mathematical Geosciences*, 49, 679–715. doi: <https://doi.org/10.1007/s11004-016-9672-8>
- Sun, W., Hui, M.-H., & Durlofsky, L. J. (2017). Production forecasting and uncertainty quantification for naturally fractured reservoirs using a new data-space inversion procedure. *Computational Geosciences*, 21, 1443–1458. doi: <https://doi.org/10.1007/s10596-017-9633-4>
- Tarantola, A. (2005). *Inverse problem theory and methods for model parameter estimation*. SIAM. doi: <https://doi.org/10.1137/1.9780898717921>
- Thibaut, R., Laloy, E., & Hermans, T. (2021). A new framework for experimental design using Bayesian Evidential Learning: The case of wellhead protection area. *Journal of Hydrology*, 603, 126903. doi: <https://doi.org/10.1016/j.jhydrol.2021.126903>
- Tian, X., Volkov, O., & Voskov, D. (2024). An advanced inverse modeling framework for efficient and flexible adjoint-based history matching of geothermal fields. *Geothermics*, 116, 102849. doi: <https://doi.org/10.1016/j.geothermics.2023.102849>
- Tso, C.-H. M., Iglesias, M., Wilkinson, P., Kuras, O., Chambers, J., & Binley, A. (2021). Efficient multiscale imaging of subsurface resistivity with uncertainty quantification using ensemble Kalman inversion. *Geophysical Journal Interna-*

- tional*, 225(2), 887–905. doi: <https://doi.org/10.1093/gji/ggab013>
- Türeyen, Ö. İ., Kırmacı, A., & Onur, M. (2014). Assessment of uncertainty in future performance predictions by lumped-parameter models for single-phase liquid geothermal systems. *Geothermics*, 51, 300–311. doi: <https://doi.org/10.1016/j.geothermics.2014.01.015>
- Williams, C. K., & Rasmussen, C. E. (2006). *Gaussian processes for machine learning*. MIT Press. doi: <https://doi.org/10.7551/mitpress/3206.001.0001>
- Wu, H., Fu, P., Morris, J. P., Mattson, E. D., Neupane, G., Smith, M. M., . . . EGS Collab Team (2021). Characterization of flow and transport in a fracture network at the EGS Collab field experiment through stochastic modeling of tracer recovery. *Journal of Hydrology*, 593, 125888. doi: <https://doi.org/10.1016/j.jhydrol.2020.125888>
- Zhang, Z., Jafarpour, B., & Li, L. (2014). Inference of permeability heterogeneity from joint inversion of transient flow and temperature data. *Water Resources Research*, 50(6), 4710–4725. doi: <https://doi.org/10.1002/2013WR013801>